Materials Advances

ROYAL SOCIETY OF CHEMISTRY

PAPER

View Article Online
View Journal | View Issue

Cite this: *Mater. Adv.*, 2024, 5, 8629

Fast preparation of adhesive, anti-freezing hydrogels with strain- and magnetic-responsive conductivities†

Xinyu He,[ab] Xinyi Huang,[ab] Shuai He,[ab] Wei Zhang,[ab] Xinhua Li,[ab] Yong You*[ab] and Fang Zuo*[ab]

Received 23rd June 2024,
Accepted 27th September 2024

DOI: 10.1039/d4ma00642a

rsc.li/materials-advances

Incorporation of magnetic components enables flexible conductive hydrogels to exhibit strain-response properties in the presence of a magnetic field. However, the utilization of flexible conductive hydrogels is constrained under low-temperature conditions, and the mechanical properties of most magnetic hydrogels are poor. In this work, a conductive sensor was developed through Ca^{2+}-initiated radical polymerization, utilizing the synergistic effects of sodium lignosulfonate (SL), calcium chloride ($CaCl_2$), and Fe_3O_4@laponites (XLG). Fe_3O_4@XLG not only served as a physical crosslinking agent but also functioned as a magnetic component. Due to the presence of both physical and chemical crosslinking, the Ca^{2+}-Fe_3O_4@XLG/SL/polyacrylamide (PAM) hydrogel had good mechanical properties. After being placed at −20 °C for 24 h, the Ca^{2+}-Fe_3O_4@XLG/SL/PAM hydrogel remained intact, soft, and tough, and it still exhibited good stretchability (1029%) and strength (69.7 kPa). In addition, the hydrogel also exhibited good adhesion with various substrates. Strain sensors assembled from the nanocomposite hydrogels achieved a gauge factor of 5.14, a response time of 166 ms, and good stability. The Ca^{2+}-Fe_3O_4@XLG/SL/PAM hydrogels had magnetic response properties, and they could respond quickly to magnetic field changes in the form of resistance changes. Thus, they have potential applications in magnetic field signal monitoring and soft actuators.

1. Introduction

Recently, flexible conductive hydrogels have attracted considerable attention due to their numerous potential applications, such as in wearable strain sensors,[1–8] electronic skin,[9–13] human motion sensors,[14–17] and soft actuators.[18–22] Within these conductive hydrogels, the strain-responsive conductivity plays a central role for their use as strain sensors. Furthermore, the introduction of magnetic units into the conductive hydrogels would broaden the application field of these hydrogels, because their conductivities would also vary in response to the magnetic fields.[23]

To avoid the effect of additional binders on the conductivities of hydrogels for auxiliary adhesion, there is an increasing demand for conductive hydrogels with adhesive properties for flexible strain sensors.[24] At present, significant progress has been made in the field of adhesive conductive hydrogels based on the unique properties of catechol and pyrogallol groups inspired by mussel adhesive protein.[25,26] Lignin is a polyphenolic biomolecule found in plants and has attracted attention in various fields due to its rich reserves, environmental friendliness, and multifunctional groups. However, because of the complexity of the molecule, lignin is not used efficiently. At present, many studies on lignin have focused on lignin derivatives, such as sodium lignosulfonate (SL) generated from the sulfite pulping process, which can endow these conductive hydrogels with an adhesive ability. Meanwhile, SL can contribute ionic conduction behavior to hydrogels. As a polymer, SL can also improve the mechanical properties through coordination and hydrogen bonding. Using SL and synthetic polymers to prepare an ionic conductive hydrogel with self-adhesion and high stretchability is a potential research topic.[27,28]

In addition, due to their high-water contents, hydrogels usually freeze, affecting their mechanical durability and ion transport capabilities.[29] Consequently, the utilization of hydrogels in extremely cold environments is severely hindered. To address this problem, incorporation of anti-freezing agents into hydrogels, including inorganic electrolytes,[30–32] zwitterionic polymers,[33–35] and polyhydric alcohols,[36] has been investigated.

[a] College of Chemistry & Environment, Southwest Minzu University, Chengdu 610041, China. E-mail: polymerzf@swun.edu.cn
[b] Key Laboratory of Pollution Control Chemistry and Environmental Functional Materials for Qinghai-Tibet Plateau of the National Ethnic Affairs Commission, Southwest Minzu University, Chengdu 610041, China

† Electronic supplementary information (ESI) available. See DOI: https://doi.org/10.1039/d4ma00642a

$CaCl_2$ is widely used to prevent ice formation on roads or house construction. Due to the physicochemical properties of $CaCl_2$, it lowers the freezing point of water,[37] thus imparting anti-freeze properties to hydrogels.[24] Ca^{2+} can also activate ammonium persulfate (APS) through electron transfer with catchol groups of SL to produce sulfate radicals ($SO_4^{\bullet -}$), which can lead to the rapid polymerization of vinyl monomers at room temperature or at low temperatures without the help of external stimuli.[24] Additionally, abundant Ca^{2+} and Cl^- would increase the conductivity of the hydrogel to act as a flexible sensor.

Magnetic-responsive hydrogels are typically prepared by incorporating magnetic particles into hydrogels. Their morphologies and properties, including deformation and movement characteristics, can be regulated remotely by manipulating the amplitude and direction of the applied magnetic field.[38] Among the magnetic materials, iron oxide nanoparticles (NPs), particularly magnetite (Fe_3O_4) NPs, are particularly popular due to their magnetic properties and biocompatibility.[39,40] However, magnetic hydrogels have some drawbacks as follows. (1) Magnetic NPs have large specific surface areas, and the free energy of the whole system is very high. According to thermodynamics, magnetic NPs in hydrogel precursors tend to self-aggregate to reduce the surface energy, resulting in the aggregation of magnetic NPs in hydrogel precursors. (2) The lack of a strong bond between the dispersed magnetic NPs and the hydrogel network can cause them to diffuse into the solution, thus affecting the structural stability of the magnetic hydrogel. LAPONITE® (XLG), a plate-like synthetic clay with a distinctive layered structure, can act as a nanoreactor and stabilizer in the synthesis of Fe_3O_4 NPs,[38,41] and it can also be used as a physical crosslinker with multiple functionalities to synthesize hydrogels with improved mechanical properties *via* hydrogen bonding and electrostatic interactions.[41,42]

This study innovatively synthesized Fe_3O_4@XLG NPs by co-precipitation method, which can not only act as a physical crosslinking agent, but also as a carrier for loading Fe_3O_4 NPs. Contributing to XLG with laminated structure can effectively prevent the aggregation of NPs, the Fe_3O_4 NPs are uniformly attached to the layered XLG surface. Therefore, the synthesis of Fe_3O_4@XLG NPs provides an effective way to improve the dispersion of magnetic NPs in hydrogels. Then we have developed a simple method to fabricate adhesive, anti-freezing, conductive, and magnetic hydrogels and explored their conductive properties in response to the strain and magnetic field. The target hydrogels were prepared by a one-pot free radical polymerization procedure, which was attributed to the redox reaction between Ca^{2+} and SL through an electron transfer process, triggering the polymerization of acrylamide (AM) monomers within minutes (Scheme 1). *N*,*N*′-Methylene bisacrylamide (BIS) acted as the chemical crosslinking, and Fe_3O_4@XLG NPs were designed as the physical crosslinks and magnetic component. SL was introduced to enhance the adhesiveness and mechanical properties. The ions from calcium chloride ($CaCl_2$), SL, and XLG worked as conductive components. The hydrogels prepared in this work are labelled as Ca^{2+}-Fe_3O_4@XLG/SL/polyacrylamide (PAM) hydrogels. The conductivity of the Ca^{2+}-Fe_3O_4@XLG/SL/PAM hydrogels exhibited both strain and magnetic responsiveness. In summary, the multifunctional hydrogel shows great potential in applications such as strain sensors, wearable devices, and magnetic actuators.

2. Experimental section

2.1 Materials

LAPONITE® (XLG) were purchased from Gangzhou Dexon Trading Co., Ltd. Iron(III) chloride hexahydrate ($FeCl_3 \cdot 6H_2O$, ≥99.0%), *N*,*N*′-methylenebis (acrylamide) (BIS, ≥98.5%) and ammonium hydroxide ($NH_3 \cdot H_2O$, ≈28%) were purchased from

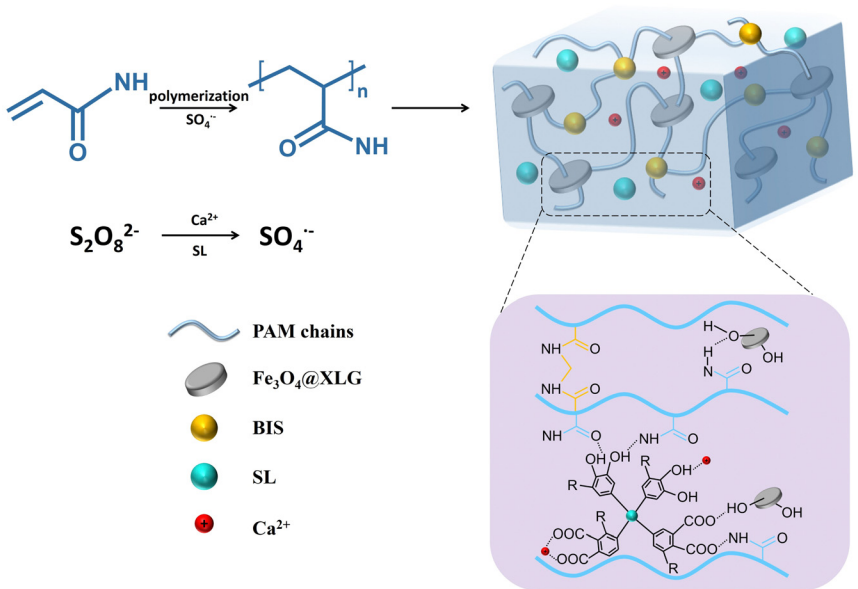

Scheme 1 Schematic illustration of fabrication process and structure of the proposed Ca^{2+}-Fe_3O_4@XLG/LS/PAM hydrogels.

Chengdu Kelon Chemical Co., Ltd. Iron(II) sulfate heptahydrate ($FeSO_4{\cdot}7H_2O$, ≥99.0%), acrylamide (AM, ≥98.0%) and ammonium persulfate (APS, ≥98.0%) were purchased from Chengdu Jinshan Chemical Reagent Co., Ltd. Calcium chloride ($CaCl_2$, ≥96.0%) was purchased from Tianjin Kemiou Chemical Reagent Co., Ltd. Sodium lignosulfonate (SL, the lignin content is 45–50%) was purchased from Shanghai Macklin Biochemical Technology Co., Ltd. Unless otherwise noted, all materials were obtained from commercial supplies and used as received without further purification.

2.2 Preparation of Fe_3O_4@XLG

Fe_3O_4@XLG nanoparticles (NPs) were synthesized by coprecipitation method. Firstly, XLG aqueous solution (15 mg mL^{-1}) was prepared by dissolving 1.5 g XLG in 100 mL deionized water. Subsequently, 4.1 g $FeCl_3{\cdot}6H_2O$ was dissolved in 80 mL XLG aqueous solution, and the above solution was poured into the flask and stirred under N_2. Nextly, 2.35 g $FeSO_4{\cdot}7H_2O$ and 20 mL XLG aqueous solution were added to the flask, and continued to stir under N_2 for 20 min. Then, 25 mL $NH_3{\cdot}H_2O$ was added and reacted at 80 °C for 1 h. Finally, the above solution was separated by the magnet after cooling and the product was washed with deionized water until the pH was 7, Fe_3O_4@XLG NPs were obtained and dispersed into 100 mL deionized water for subsequent operation. The concentration of Fe_3O_4@XLG NPs in Fe_3O_4@XLG NPs aqueous solution was 22.7 mg mL^{-1}.

2.3 Preparation of Ca^{2+}-Fe_3O_4@XLG/SL/PAM hydrogel

Firstly, 0.5 g AM was dissolved in 2 mL Fe_3O_4@XLG NPs aqueous solution. Subsequently, 0.05 mL SL (0.245 mol), 0.1 mL $CaCl_2$ (0.555 mol), 0.4 mL BIS and 0.2 mL APS (2.282 mol) were added successively under an ice bath, and ultrasonic stirred for 15 s after each addition. Finally, the above solution was injected into the mold and Ca^{2+}-Fe_3O_4@XLG/SL/PAM hydrogel was formed after 1 h. Ca^{2+}-Fe_3O_4@XLG/SL/PAM hydrogels with different raw material ratios were prepared by the same method.

2.4 Preparation of Fe^{3+}-Fe_3O_4@XLG/SL/PAM hydrogel and SL/PAM hydrogel

As a control, Fe^{3+}-Fe_3O_4@XLG/SL/PAM hydrogel was synthesized using the same method by simply replacing Ca^{2+} with Fe^{3+}. The dosages of AM, Fe_3O_4@XLG, SL, BIS, and APS in Fe^{3+}-Fe_3O_4@XLG/SL/PAM hydrogel were all consistent with those in Ca^{2+}-Fe_3O_4@XLG/SL/PAM hydrogel.

Pristine SL/PAM hydrogel was synthesized without Fe_3O_4@XLG by traditional free radical polymerization of AM in the presence of APS at 60 °C for 4 h. The dosages of AM, SL, BIS and APS in SL/PAM hydrogel were all consistent with those in Ca^{2+}-Fe_3O_4@XLG/SL/PAM hydrogel, and the total volume was kept consistent.

2.5 Mechanical test

The mechanical properties of hydrogels were assessed using a universal tensile machine (QX-W200, Shanghai Qixiang Testing Instrument Co., Ltd). The hydrogels utilized in the experiment were cylindrical, measuring 4.5 mm in diameter and 30 mm in length. The stretching velocity remained constant at 100 mm min^{-1}. The experiments were repeated 3 times and the average value was recorded. The tensile strength is defined as:

$$\sigma = F/A_0 \quad (1)$$

where σ is the tensile strength (Pa), F is the tensile load (N), A_0 is the initial cross-sectional area of the hydrogels (m^2).

2.6 Adhesion test

The adhesion properties of Ca^{2+}-Fe_3O_4@XLG/SL/PAM hydrogel were evaluated using the lap-shear test. Two substrates were adhered together using the hydrogel, creating a bonding area of 10 × 10 mm^2. The pressure was applied at 1 kPa for 10 s in ambient air without any additional treatment, followed by immediate removal of the external pressure. The peak stress observed during shear adhesive tests was documented as the adhesive strength, determined by dividing the maximum force by the initial bonding area.

2.7 Electrical properties test

The resistance of hydrogel was assessed using the compact LCR digital bridge TH283X. The sensitivity of the strain sensor is typically assessed based on the gauge factor (GF), which was estimated as follows:

$$GF = (\Delta R/R_0)/\varepsilon \quad (2)$$

where ΔR is the measured resistance (R) minus the initial resistance (R_0), and ε is the applied strain.

2.8 Microscopic morphology test

The microscopic morphology of the NPs was characterized using a transmission electron microscope (TEM, FEI Tecnai G2F 20, America) at 200 kV by dispersing XLG and Fe_3O_4@XLG NPs on the copper network.

2.9 Crystalline structure test

The crystalline structure of XLG and Fe_3O_4@XLG NPs was characterized by X-ray diffractometer (XRD, XD-6, Beijing Pu-Analysis General Instrument Co., Ltd, China) with Cu K radiation in the range of 5°–90°.

2.10 Zeta potential test

The zeta potential of the NPs was obtained by MALVERN, ZEN3690/MPT-2. The XLG and Fe_3O_4@XLG NPs were dispersed in deionized water and uniformly dispersed by sonication, and 700 μL of the solution was placed in the potential cuvette.

3. Results and discussion

3.1 Characterization of Fe_3O_4@XLG

In the preparation of hydrogels, XLG is often used solely as the physical crosslinking agent. The hydroxyl groups and surface charges on the XLG facilitate physical interactions, such as

hydrogen bonding and electrostatic interactions, with the polymer chains.[43] This leads to the development of a hydrogel with an enhanced toughness and stretchability, thereby imparting effective mechanical properties. In fact, XLG can also function as a carrier for loading Fe_3O_4 nanoparticles (NPs), because XLG with a lamellar stack structure could prevent NPs from aggregating.

Fig. 1a and b show transmission electron microscopy images of the XLG and Fe_3O_4@XLG NPs, respectively. It can be seen that Fe_3O_4 NPs were attached to the layered XLG surface. Fig. 1c shows the average size of the nanoparticles. It can be seen that the specific size of XLG is about 33 nm, and the specific size of Fe_3O_4@XLG is about 106 nm, which further indicated that the Fe_3O_4 NPs were attached to the layered XLG surface and multiple layers of XLG contacted with one another at presence of the Fe_3O_4 NPs. In addition, the corresponding difference of the zeta potentials of XLG and Fe_3O_4@XLG NPs indicated that there were interactions between the Fe_3O_4 NPs and XLG (Fig. S1, ESI†). As shown in Fig. 1d, the XRD spectra of the Fe_3O_4@XLG NPs contained the characteristic diffraction peaks of Fe_3O_4 NPs (JCPDS No. 19-0629) and partial peaks of XLG. It is clearly that Fe_3O_4@XLG NPs have obvious diffraction peaks at 2θ of 30.0°, 35.4°, 43.0°, 56.9° and 62.5°, which mainly correspond to the (110), (311), (400), (511) and (440) crystal planes of the Fe_3O_4 NPs, respectively. This result show that a multi-component nanohybrid has been successfully prepared. Compared to pure XLG, the diffraction peak of XLG in the Fe_3O_4@XLG NPs was significantly weakened, indicating that the diffraction peak of XLG was covered by that of Fe_3O_4 in the magnetic composite NPs, which was also consistent with the results of Fig. 1b. As shown in Fig. S2 (ESI†), Fe_3O_4@XLG NPs exhibited a typical hysteresis loop in its magnetic behavior. There was no coercivity or remanence in the obtained test curves, indicating that Fe_3O_4@XLG NPs were superparamagnetic, and the maximum saturation magnetization (M_s) was found to be 41.6 emu g^{-1}.

The above results showed that Fe_3O_4@XLG NPs with good magnetic properties were successfully synthesized. In our work, Fe_3O_4@XLG NPs were incorporated into the hydrogel as both the magnetic component and the physical crosslinker.

3.2 Mechanical properties of the Ca^{2+}-Fe_3O_4@XLG/SL/PAM hydrogel

Metal ions can activate ammonium persulfate (APS) through electron transfer to produce sulfate radicals ($SO_4^{\bullet -}$). The mechanical properties of the hydrogels synthesized by APS triggered by Ca^{2+} and other metal ions were compared. Fig. 2a shows the comparison of the mechanical properties of the Fe^{3+}-Fe_3O_4@XLG/SL/PAM and Ca^{2+}-Fe_3O_4@XLG/SL/PAM hydrogels. The strain (765%) and tensile strength (114.4 kPa) of the Ca^{2+}-Fe_3O_4@XLG/SL/PAM hydrogel were much larger than those of the Fe^{3+}-Fe_3O_4@XLG/SL/PAM hydrogel, which was due to the different catalytic efficiencies of different metal ions. The catalytic efficiency of Fe^{3+} was higher than that of Ca^{2+}, which led to a faster polymerization rate.[44] Consequently, the Fe-based hydrogel had short polymer chains, resulting in weak mechanical properties.[44]

The reaction system was supplemented with the chemical crosslinking agent BIS and the physical crosslinking agent XLG, enabling the modulation of the hydrogel crosslinking density. Composite hydrogels with different mechanical properties were obtained by changing the contents of BIS and XLG. As shown in Fig. 2c, the strain of the Ca^{2+}-Fe_3O_4@XLG/SL/PAM hydrogel decreased significantly when the content of BIS increased. The increase in the concentration of the chemical crosslinking agent BIS could enhance the crosslinking density of the crosslinking network, which led to a decrease in the strain at break of the hydrogel. When the content of BIS was lower than 0.001 g mL^{-1}, the hydrogel could not form. Therefore, 0.001 g mL^{-1} BIS was used for subsequent experiments. The Ca^{2+}-Fe_3O_4@XLG/SL/PAM

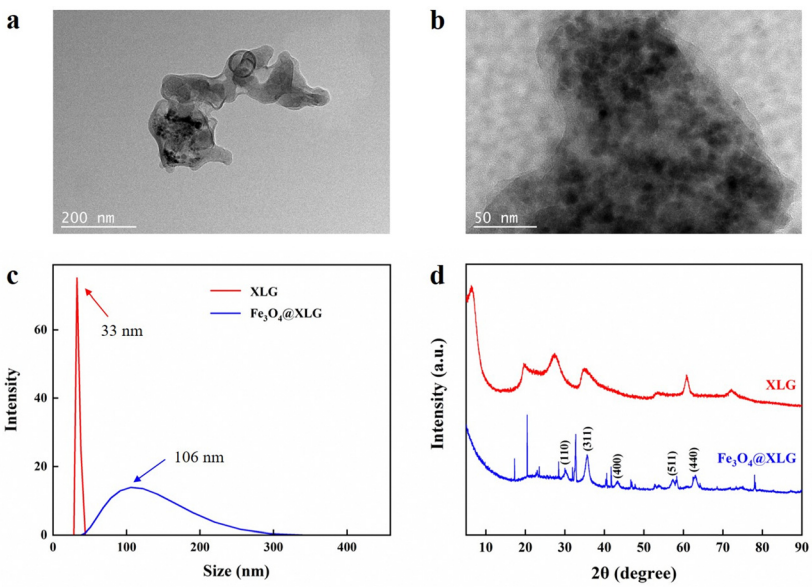

Fig. 1 The TEM images of (a) XLG and (b) Fe_3O_4@XLG NPs. (c) The size and (d) XRD spectra of XLG and Fe_3O_4@XLG NPs.

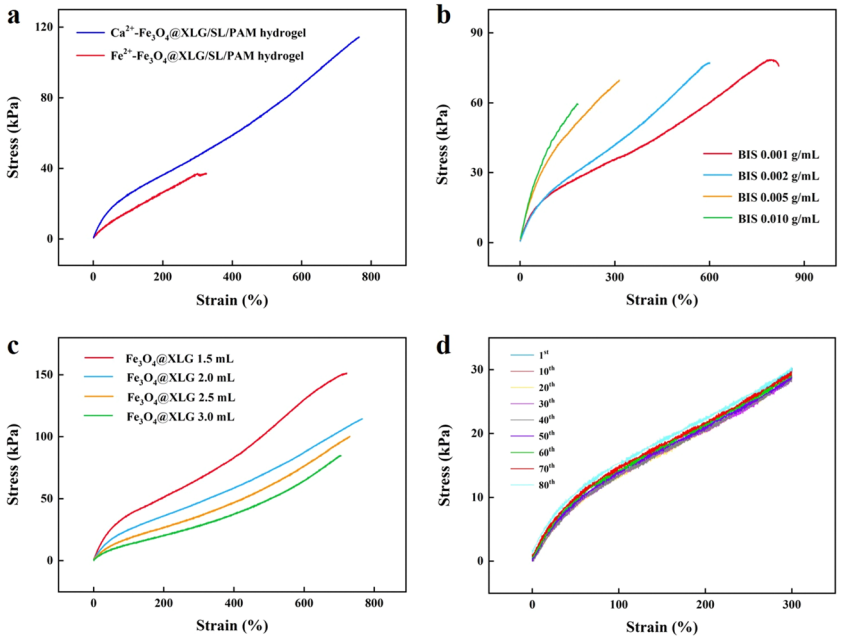

Fig. 2 Mechanical properties of the Ca^{2+}-Fe_3O_4@XLG/SL/PAM hydrogel. (a) Stress–strain curves of the Ca^{2+}-Fe_3O_4@XLG/SL/PAM hydrogel and the Fe^{3+}-Fe_3O_4@XLG/SL/PAM hydrogel. Stress–strain curves of the Ca^{2+}-Fe_3O_4@XLG/SL/PAM hydrogel with different dosage of (b) BIS and (c) Fe_3O_4@XLG. (d) Elasticity of the Ca^{2+}-Fe_3O_4@XLG/SL/PAM hydrogel under 80 successive loading–unloading cycles.

hydrogel exhibited a suitable tensile strength (75.7 kPa) and stretchability (819%) at the BIS content of 0.001 g mL^{-1}. Because XLG in the system only came from the Fe_3O_4@XLG, the dosage of XLG was adjusted by changing the dosage of Fe_3O_4@XLG. Fig. 2b shows the stress–strain curves of the Ca^{2+}-Fe_3O_4@XLG/SL/PAM hydrogel with different dosages of Fe_3O_4@XLG. As the dosage of Fe_3O_4@XLG was increased, the strain did not change significantly, but the intensity was greatly reduced. The crosslinking point of the hydrogels increased rapidly and became too dense when the XLG content reached a certain amount. The excessive crosslinking restricted the movement of the polymer chains, resulting in lower breaking stresses. The dosage of Fe_3O_4@XLG directly affected the magnetic properties of the hydrogel. Therefore, considering the magnetic properties and mechanical properties, 2 mL of Fe_3O_4@XLG was used for subsequent experiments. The Ca^{2+}-Fe_3O_4@XLG/SL/PAM hydrogel exhibited a good tensile strength (114.4 kPa) and stretchability (765%) at the Fe_3O_4@XLG dosage of 2 mL.

Stability is crucial for the practical application of hydrogels. Therefore, we characterized the fatigue properties of the Ca^{2+}-Fe_3O_4@XLG/SL/PAM hydrogel. As shown in Fig. 2d, the Ca^{2+}-Fe_3O_4@XLG/SL/PAM hydrogel showed only weak hysteresis in the stress–strain curves even after 80 cycles of continuous tension recovery testing, with a tensile deformation of 300%. This indicated that the Ca^{2+}-Fe_3O_4@XLG/SL/PAM hydrogel had good fatigue resistance. On the one hand, this may have been due to the hydrogen bonding interactions between the –SiOH groups on the XLG, the $–NH_2$ groups on the PAM chains, and the –OH groups on the SL, which could recover quickly after being damaged. The metal coordination interactions provided by Ca^{2+} and the presence of electrostatic interactions in this system were also important to the anti-fatigue properties. On the other hand, in general, the magnetic NPs tended to agglomerate when the magnetic hydrogels were stretched, which affected the mechanical properties. In the Ca^{2+}-Fe_3O_4@XLG/SL/PAM hydrogel, Fe_3O_4 NPs were uniformly dispersed on the XLG layer, and agglomeration would not occur when the hydrogel was deformed by an external force. As a result, the hydrogel exhibited good anti-fatigue performances. These results indicated that the Ca^{2+}-Fe_3O_4@XLG/SL/PAM hydrogel had good mechanical properties.

3.3 Anti-freezing properties of the Ca^{2+}-Fe_3O_4@XLG/SL/PAM hydrogel

Conventional hydrogels freeze at low temperatures, which severely limits their applications, such as in sensors. Fig. 3a and b show the comparison of the shapes and morphologies of the Ca^{2+}-Fe_3O_4@XLG/SL/PAM hydrogel and pristine SL/PAM hydrogel placed at −20 °C for 24 h. It was clear that the SL/PAM hydrogel became both opaque and hard, completely losing flexibility, ductility, and adhesion. In contrast, the Ca^{2+}-Fe_3O_4@XLG/SL/PAM hydrogel remained intact, soft, and tough, and it could still be stretched to approximately eight times its initial length. At the precence of Ca^{2+}, the water molecules leaving the solid phase will slow down when the temperature decreases. And the rate will eventually match the rate at which water molecules form a solid in the presence of a salt, and a lower freezing point is established.[45] $CaCl_2$ lowers the freezing point of the aqueous phase, weakens the hydrogen bonds within water molecules, disrupts the aggregation of these molecules, and effectively impedes the formation of ice crystals within the hydrogel.[45] Consequently, the

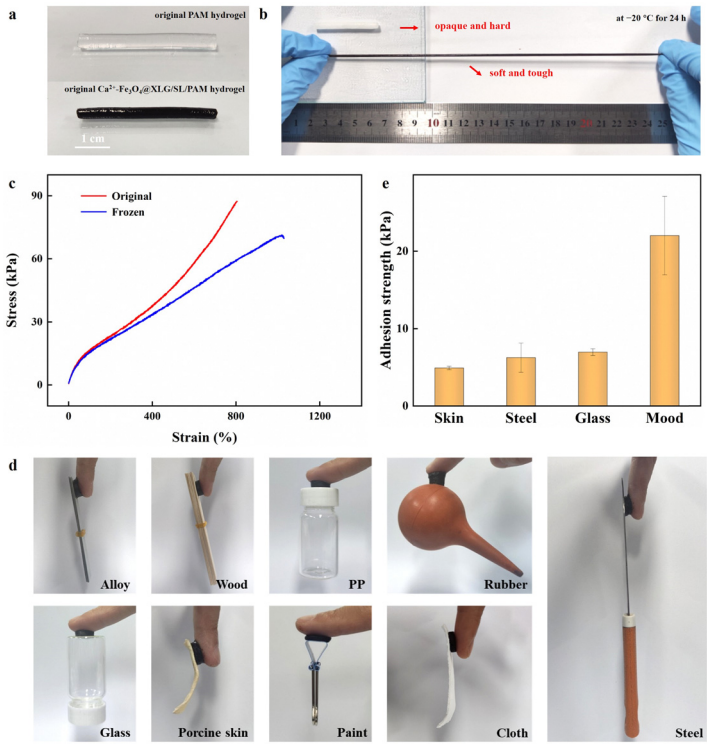

Fig. 3 (a) The original state of the SL/PAM hydrogel and the Ca^{2+}-Fe_3O_4@XLG/SL/PAM hydrogel. (b) The comparison of the shape and morphology of the hydrogel placed at −20 °C for 24 h. (c) The stress–strain curve of the Ca^{2+}-Fe_3O_4@XLG/SL/PAM hydrogel placed at −20 °C for 24 h. (d) The Ca^{2+}-Fe_3O_4@XLG/SL/PAM hydrogel showed good adhesion to various substrates. (e) The adhesion strength of the Ca^{2+}-Fe_3O_4@XLG/SL/PAM hydrogel on different substrates.

Ca^{2+}-Fe_3O_4@XLG/SL/PAM hydrogel exhibited anti-freezing properties due to the addition of $CaCl_2$.

The mechanical properties of the Ca^{2+}-Fe_3O_4@XLG/SL/PAM hydrogel after freezing at −20 °C for 24 h were further characterized. As shown in Fig. 3c, the stress–strain curve indicated that the mechanical properties of the Ca^{2+}-Fe_3O_4@XLG/SL/PAM hydrogel had undergone some changes after freezing, but it still exhibited a suitable tensile strength (69.7 kPa) and strain (1029%). This confirmed the excellent flexibility of the hydrogels at low temperatures, which would ensure their applicability under extremely cold environments.

3.4 Adhesion properties of the Ca^{2+}-Fe_3O_4@XLG/SL/PAM hydrogel

The presence of Na^+ of the SL in the network could contribute to certain conductive properties. Additionally, the catechol groups on the SL could engage in diverse covalent and non-covalent interactions with the matrix.[46,47] Therefore, the self-adhesive properties of the Ca^{2+}-Fe_3O_4@XLG/SL/PAM hydrogel avoided the effect of using additional adhesives on the conductivity of the hydrogel. The hydrogel could adhere to the surfaces of an alloy, wood, polypropylene (PP), glass, steel, cloth, porcine skin, rubber, and paint (Fig. 3d). The adhesion strengths of the Ca^{2+}-Fe_3O_4@XLG/SL/PAM hydrogel on porcine skin, steel, glass, and wood are shown in the Fig. 3e. The high adhesion strength to wood could be attributed to the rough, porous structure and polyhydroxy structure of the wood, which was conducive to the infiltration of the hydrogel and hydrogen bond formation. The adhesion of the Ca^{2+}-Fe_3O_4@XLG/SL/PAM hydrogel could be attributed to the synergistic effect of various covalent and non-covalent interactions between the rich catechol groups of SL and the substrate.[28,47,48] Catechol groups from the introduced LS interact with various substrates through hydrogen bonds, coordination bonds, cation–π interactions, π–π interactions, and covalent linking, resulting in a desirable adhesiveness of the Ca^{2+}-Fe_3O_4@XLG/SL/PAM hydrogel.

3.5 Strain-responsive conductivity properties of the Ca^{2+}-Fe_3O_4@XLG/SL/PAM hydrogel

SL contained Na^+, which also made the hydrogel conductive. However, due to the low content of SL, it provided a limited electrical conductivity. The enhanced conductivity of the Ca^{2+}-Fe_3O_4@XLG/SL/PAM hydrogel was primarily attributed to the incorporation of $CaCl_2$, resulting in a remarkable conductivity value of 3.46 S m^{-1}. The Ca^{2+}-Fe_3O_4@XLG/SL/PAM hydrogel was connected to the resistance test system, and the resistance changes of the hydrogel when stretched to different strains are shown in Fig. 4a. The results indicated that as the hydrogel was stretched continuously, its resistance increased immediately with hardly any hysteresis. When the hydrogel returned to its initial length, the resistance immediately decreased to its initial value. The sensitivity of a flexible sensor is usually evaluated by the gauge factor (GF, $(\Delta R/R_0)/\varepsilon$). As the strain was increased to 100%, the GF was found to be 5.14,

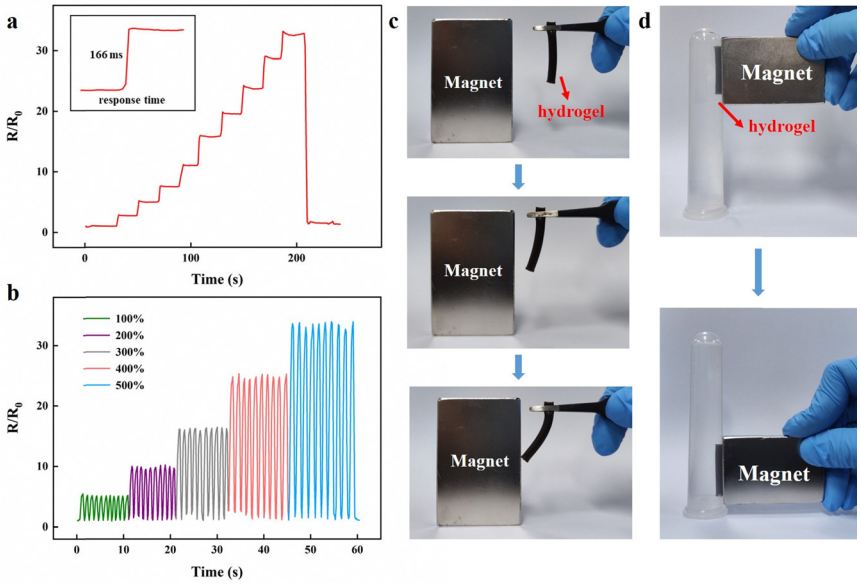

Fig. 4 (a) The resistance change of the Ca^{2+}-Fe_3O_4@XLG/SL/PAM hydrogel under different tensile strain. (b) Stability tests of the Ca^{2+}-Fe_3O_4@XLG/SL/PAM hydrogel when repeatedly stretched. (c) and (d) Magnetic responsive properties of the Ca^{2+}-Fe_3O_4@XLG/SL/PAM hydrogel.

which indicated that the Ca^{2+}-Fe_3O_4@XLG/SL/PAM hydrogel was capable of responding to minor deformations. In addition, the response time of the Ca^{2+}-Fe_3O_4@XLG/SL/PAM hydrogel was only 166 ms. It can be seen from Fig. 4b that the resistance changed regularly when the Ca^{2+}-Fe_3O_4@XLG/SL/PAM hydrogel was repeatedly stretched, and it had good stability. Therefore, the Ca^{2+}-Fe_3O_4@XLG/SL/PAM hydrogel had a certain sensing range, sensitivity, and stability. It could capture very small deformations and quickly respond to deformation (166 ms).

3.6 Magnetic responsive properties of the Ca^{2+}-Fe_3O_4@XLG/SL/PAM hydrogel

Due to the incorporation of Fe_3O_4@XLG NPs, the Ca^{2+}-Fe_3O_4@XLG/SL/PAM hydrogel exhibited magnetic properties. As shown in Fig. 4c, the Ca^{2+}-Fe_3O_4@XLG/SL/PAM hydrogel maintained a vertical state under the action of gravity. When the magnet was close to the hydrogel, the lower end of the hydrogel was deflected under the action of the magnetic field. As shown in Fig. 4d, the Ca^{2+}-Fe_3O_4@XLG/SL/PAM hydrogel moved up and down in water when attracted by the magnet.

The Ca^{2+}-Fe_3O_4@XLG/SL/PAM hydrogel exhibited a certain conductivity, magnetic responsiveness, flexibility, and fatigue resistance. This work attempted to manipulate the magnetic hydrogel to produce deformation by changing the strength of the magnetic field. As shown in Fig. 5a, the Ca^{2+}-Fe_3O_4@XLG/SL/PAM hydrogel was deformed by the attraction of the magnet. The resistance of the hydrogel increased immediately due to deformation, and this process could be repeated, as shown in Fig. 5b. The hydrogel recovered to its original state as the magnet moved away, and the resistance was also restored to the initial value. The results indicated that the Ca^{2+}-Fe_3O_4@XLG/SL/PAM hydrogel is promising for magnetic field signal monitoring.

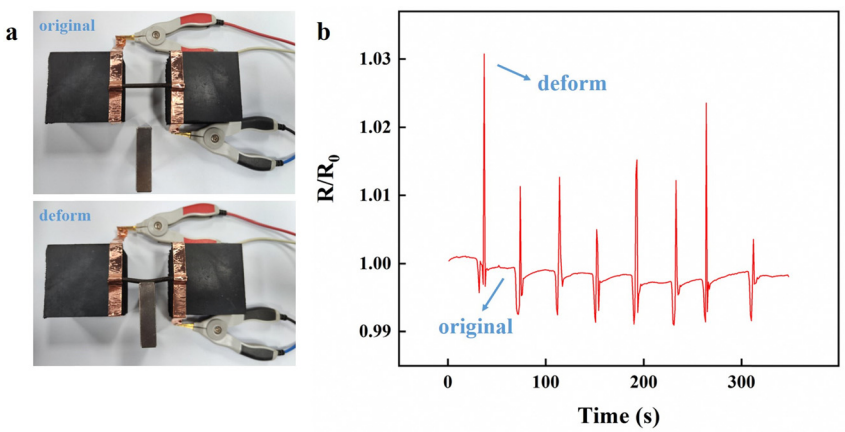

Fig. 5 (a) The Ca^{2+}-Fe_3O_4@XLG/SL/PAM hydrogel deformed under the external magnetic field. (b) Cyclic resistance change rate-time curves of the Ca^{2+}-Fe_3O_4@XLG/SL/PAM hydrogel.

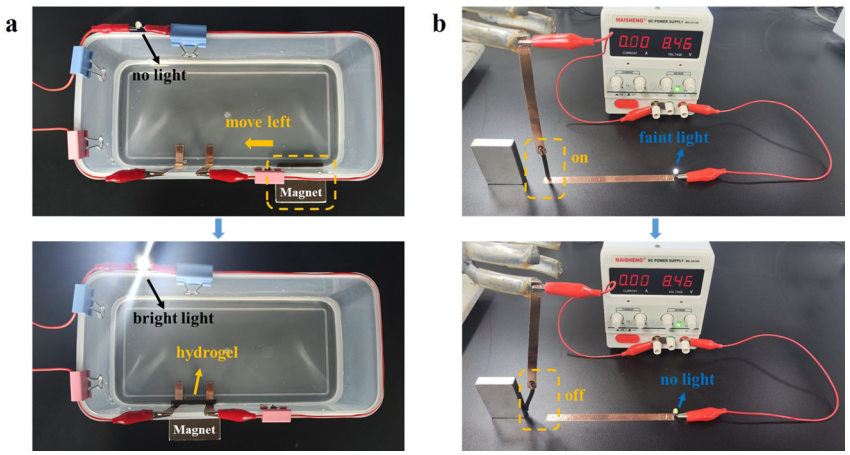

Fig. 6 (a) The Ca^{2+}-Fe_3O_4@XLG/SL/PAM hydrogel connected the circuit in a non-contact form under the attraction of the external magnetic field. (b) The Ca^{2+}-Fe_3O_4@XLG/SL/PAM hydrogel can control the disconnection and connection of circuits by applying a magnetic field.

3.7 Soft actuator based on the Ca^{2+}-Fe_3O_4@XLG/SL/PAM hydrogel

The remarkable feature of the magnetic hydrogel was its ability to change its shape and position under remote control. Therefore, the Ca^{2+}-Fe_3O_4@XLG/SL/PAM hydrogel has the potential for application in soft actuators. In this work, the Ca^{2+}-Fe_3O_4@XLG/SL/PAM hydrogel was used to connect the circuit in a non-contact form under the traction of the external magnetic field. The following device was constructed to simulate the process of the Ca^{2+}-Fe_3O_4@XLG/SL/PAM hydrogel being connected to a circuit under magnetic field traction, as shown in Fig. 6a. The hydrogel and magnet were placed on the right side of the device, and two non-touching copper strips on the left of the device simulated a disconnected circuit. The hydrogel and copper strips were placed in deionized water. Under the attraction of the magnet, the Ca^{2+}-Fe_3O_4@XLG/SL/PAM hydrogel immediately moved to the left onto the copper strips and connected the disconnected circuit to form a closed circuit, at which time the LED lit up. Moreover, the above device was mounted in water and could still function, which indicated that the Ca^{2+}-Fe_3O_4@XLG/SL/PAM hydrogel has various application scenarios in the field of soft actuators. As shown in Fig. 6b, the hydrogel was connected to the closed circuit, and the LED lit up. The hydrogel was then attracted by the magnet, which caused the circuit to break, at which time the LED light went out. In summary, the Ca^{2+}-Fe_3O_4@XLG/SL/PAM hydrogel could be used as soft actuator to control the disconnection and connection of circuits due to its conductivity and magnetic properties.

4. Conclusions

In this study, we reported a one-pot free radical polymerization procedure to fabricate adhesive, anti-freezing hydrogels with strain and magnetic responsive conductivities. The Ca^{2+}-Fe_3O_4@XLG/SL/PAM hydrogel was prepared by the free radical polymerization of AM through electron transfer, induced by the redox reaction between Ca^{2+} and SL. SL also played as a role of the adhesive component. The Ca^{2+}-Fe_3O_4@XLG/SL/PAM hydrogel exhibited good flexibility and fatigue resistance due to the physical crosslinking of XLG and the chemical crosslinking of BIS. In addition, the conductive hydrogels exhibited good adhesion properties to various substrates. The hydrogel remained intact, soft, and tough after 24 h at −20 °C, and it still exhibited a suitable tensile strength (69.7 kPa) and strain at break (1029%). The Ca^{2+}-Fe_3O_4@XLG/SL/PAM hydrogel could be successfully used as a strain sensor with large ranges, a high GF, a short response time, and good stability. The hydrogel also showed magnetic response properties due to the addition of Fe_3O_4@XLG, and it responded quickly to magnetic field changes in the form of resistance changes. Based on these advantages, the flexible conductive Ca^{2+}-Fe_3O_4@XLG/SL/PAM hydrogel could be applied for magnetic field signal monitoring and soft actuators, and it could function in extremely cold conditions.

Data availability

The data that support the findings of this study are available from the corresponding author, upon reasonable request.

Conflicts of interest

The authors declare that they have no known competing financial interests or personal relationships that could have appeared to influence the work reported in this paper.

Acknowledgements

This work was supported by the National Natural Science Foundation of China (51273220), and Innovative Research Projects for Graduate Students, Southwest Minzu University (ZD2022695). We thank LetPub (https://www.letpub.com/) for its linguistic assistance during the preparation of this manuscript.

References

1 J. Zhang, Q. Zhang, X. Liu, S. Xia, Y. Gao and G. Gao, *J. Polym. Sci.*, 2022, **60**, 2663–2678.
2 S. Ko, A. Chhetry, D. Kim, H. Yoon and J. Park, *ACS Appl. Mater. Interfaces*, 2022, **14**, 31363–31372.
3 X. He, N. Wen, W. Zhang, S. He, S. Yang, X. Li, C. Chen and F. Zuo, *RSC Adv.*, 2023, **13**, 7561–7568.
4 W. Zhang, L. Xu, M. Zhao, Y. Ma, T. Zheng and L. Shi, *Soft Matter*, 2022, **18**, 1644–1652.
5 S. Li, Z. Yu, B. Guo, K. Guo, Y. Li, L. Gong, L. Zhao, J. Bae and L. Tang, *Nano Energy*, 2021, **90**, 106502.
6 S. Li, X. He, Z. Zeng, B. Jiang, Q. Wu, L. Gong, Y. Li, J. Bae, S. Wang and L. Tang, *Nano Energy*, 2022, **103**, 107789.
7 Z. Zeng, Y. Yang, X. Pang, B. Jiang, L. Gong, Z. Liu, L. Peng and S. Li, *Adv. Funct. Mater.*, 2024, 2409855.
8 H. Zhou, J. Lai, B. Zheng, X. Jin, G. Zhao, H. Liu, W. Chen, A. Ma, X. Li and Y. Wu, *Adv. Funct. Mater.*, 2021, **32**, 2108423.
9 Y. Lu, X. Qu, S. Wang, Y. Zhao, Y. Ren, W. Zhao, Q. Wang, C. Sun, W. Wang and X. Dong, *Nano Res.*, 2021, **15**, 4421–4430.
10 Q. Peng, J. Chen, T. Wang, X. Peng, J. Liu, X. Wang, J. Wang and H. Zeng, *InfoMat*, 2020, **2**, 843–865.
11 W. Li, J. Liu, J. Wei, Z. Yang, C. Ren and B. Li, *Adv. Funct. Mater.*, 2023, **33**, 2213485.
12 Q. Yu, Z. Zheng, X. Dong, R. Cao, S. Zhang, X. Wu and X. Zhang, *Soft Matter*, 2021, **17**, 8786–8804.
13 B. Zheng, H. Zhou, Z. Wang, Y. Gao, G. Zhao, H. Zhang, X. Jin, H. Liu, Z. Qin, W. Chen, A. Ma, W. Zhao and Y. Wu, *Adv. Funct. Mater.*, 2023, **33**, 2213501.
14 W. Dai, J. Wang, K. Xiang, W. Hu, J. Sun, H. Zhang and L. Wang, *ACS Appl. Mater. Interfaces*, 2023, **15**, 29499–29510.
15 L. Dong, M. Wang, J. Wu, C. Zhu, J. Shi and H. Morikawa, *ACS Appl. Mater. Interfaces*, 2022, **14**, 9126–9137.
16 Z. Wang, Y. Cong and J. Fu, *J. Mater. Chem. B*, 2020, **8**, 3437–3459.
17 H. Zhou, Z. Jin, Y. Gao, P. Wu, J. Lai, S. Li, X. Jin, H. Liu, W. Chen, Y. Wu and A. Ma, *Colloids Surf., A*, 2022, **636**, 128113.
18 P. Xue, C. Valenzuela, S. Ma, X. Zhang, J. Ma, Y. Chen, X. Xu and L. Wang, *Adv. Funct. Mater.*, 2023, **33**, 2214867.
19 S. Maiz-Fernández, L. Pérez-Álvarez, U. Silván, J. Vilas-Vilela and S. Lanceros-Méndez, *Polymers*, 2022, **14**, 650.
20 X. Dong, X. Luo, H. Zhao, C. Qiao, J. Li, J. Yi, L. Yang, F. Oropeza, T. Hu, Q. Xu and H. Zeng, *Soft Matter*, 2022, **18**, 7699–7734.
21 P. Wu, H. Zhou, Y. Gao, Y. Chen, K. Wang, C. Wei, H. Zhang, X. Jin, A. Ma, W. Chen and H. Liu, *J. Colloid Interface Sci.*, 2024, **662**, 976–985.
22 Y. Gao, H. Zhou, B. Zheng, Z. Wang, G. Zhao, H. Zhang, H. Liu, X. Jin, W. Chen, A. Ma and Y. Wu, *Chem. Eng. J.*, 2023, **465**, 142923.
23 A. Puiggalí-Jou, I. Babeli, J. Roa, J. Zoppe, J. Garcia-Amorós, M. Ginebra, C. Alemán and J. García-Torres, *ACS Appl. Mater. Interfaces*, 2021, **13**, 42486–42501.
24 H. Lv, S. Zong, T. Li, Q. Zhao, Z. Xu and J. Duan, *ACS Omega*, 2023, **8**, 9434–9444.
25 J. Ren, M. Zhang, M. Li, R. Li, Y. Li and W. Yang, *New J. Chem.*, 2023, **47**, 16148–16159.
26 W. Zhang, Z. Liao, X. Meng, A. Ai Niwaer, H. Wang, X. Li, D. Liu and F. Zuo, *Appl. Surf. Sci.*, 2020, **527**, 146821.
27 Y. Wang, H. Liu, X. Ji, Q. Wang, Z. Tian and S. Liu, *Int. J. Biol. Macromol.*, 2022, **212**, 393–401.
28 C. Fu, X. Liu, Y. Yi, P. Fatehi, X. Meng, F. Kong and S. Wang, *Polym. Test.*, 2022, **107**, 107486.
29 A. Mondal, D. Xu, S. Wu, Q. Zou, W. Lin, F. Huang and Y. Ni, *Int. J. Biol. Macromol.*, 2022, **214**, 77–90.
30 Y. Song, L. Niu, P. Ma, X. Li, J. Feng and Z. Liu, *ACS Appl. Mater. Interfaces*, 2023, **15**, 10006–10017.
31 Y. Liu, Q. Liu, L. Zhong, C. Chen and Z. Xu, *Chem. Eng. J.*, 2023, **452**, 139314.
32 L. Shu, Z. Wang, X. Zhang and J. Yao, *Int. J. Biol. Macromol.*, 2023, **230**, 123425.
33 Y. Zhao, N. Yang, X. Chu, F. Sun, M. Ali, Y. Zhang, B. Yang, Y. Cai, M. Liu, N. Gasparini, J. Zheng, C. Zhang, C. Guo and H. Meng, *Adv. Mater.*, 2023, **35**, 2211617.
34 Y. Wang, H. Liu, J. Yu, H. Liao, L. Yang, E. Ren, S. Lin and J. Lan, *Biomacromolecules*, 2024, **25**, 838–852.
35 S. Xue, Y. Wu, M. Guo, Y. Xia, D. Liu, H. Zhou and W. Lei, *Soft Matter*, 2019, **15**, 3680–3688.
36 J. Zhang, Y. Wang, Q. Wei, M. Li and X. Chen, *J. Colloid Interface Sci.*, 2024, **653**, 1514–1525.
37 X. Zhang, X. Ma, T. Hou, K. Guo, J. Yin, Z. Wang, L. Shu, M. He and J. Yao, *Angew. Chem., Int. Ed.*, 2019, **58**, 7366–7370.
38 J. Lee, W. Han, H. Jang and H. Choi, *Sci. Rep.*, 2019, **9**, 15024.
39 J. Sun, S. Zhou, P. Hou, Y. Yang, J. Weng, X. Li and M. Li, *J. Biomed. Mater. Res., Part A*, 2006, **80A**, 333–341.
40 D. Chen, Q. Tang, X. Li, X. Zhou, J. Zang, W. Xue, J. Xiang and C. Guo, *Int. J. Nanomed.*, 2012, **7**, 4973–4982.
41 O. Goncharuk, Y. Samchenko, L. Kernosenko, O. Korotych, T. Poltoratska, N. Pasmurtseva, O. Oranska, D. Sternik and I. Mamyshev, *Soft Matter*, 2020, **16**, 5689–5701.
42 L. Selzer and S. Odenbach, *Gels*, 2023, **9**, 182.
43 B. Gao, H. Yu, J. Wen, H. Zeng, T. Liang, F. Zuo and C. Cheng, *J. Environ. Chem. Eng.*, 2021, **9**, 106346.
44 Z. Jia, Y. Zeng, P. Tang, D. Gan, W. Xing, Y. Hou, K. Wang, C. Xie and X. Lu, *Chem. Mater.*, 2019, **31**, 5625–5632.
45 X. Zhang, K. Wang, J. Hu, Y. Zhang, Y. Dai and F. Xia, *J. Mater. Chem. A*, 2020, **8**, 25390–25401.
46 A. Mondal, S. Wu, D. Xu, Q. Zou, L. Chen, L. Huang, F. Huang and Y. Ni, *Int. J. Biol. Macromol.*, 2021, **187**, 189–199.
47 J. Cao, Y. Zhao, S. Jin, J. Li, P. Wu and Z. Luo, *Chem. Eng. J.*, 2022, **429**, 132252.
48 Z. Liao, W. Zhang, Z. Qiao, J. Luo, A. Ai Niwaer, X. Meng, H. Wang, X. Li, F. Zuo and Z. Zhao, *J. Colloid Interface Sci.*, 2020, **562**, 81–90.